



# Computer Modeling of Wind Turbines: 2. Free-Surface FSI and Fatigue-Damage

Yuri Bazilevs<sup>1</sup> · Jinhui Yan<sup>2</sup> · Xiaowei Deng<sup>3</sup> · Artem Korobenko<sup>4</sup>

Received: 26 June 2018 / Accepted: 1 September 2018 / Published online: 14 September 2018  
© CIMNE, Barcelona, Spain 2018

## Abstract

This article reviews state-of-the-art numerical techniques for fluid–structure interaction (FSI) of full-scale wind-turbine systems. Simulation of floating wind turbines subjected to combined wind-flow and ocean-wave forcing, and modeling of high-cycle fatigue failure of blades due to long-term cyclic aerodynamic loading, are the focal points of this article. Computational techniques including advanced structural modeling based on Isogeometric Analysis, free-surface FSI, and fatigue-damage modeling, are presented. Representative computational examples involving land-based and floating offshore wind-turbine designs illustrate the versatility and power of the computational methods developed.

## 1 Introduction

### 1.1 Offshore Wind and the Need for Advanced Simulation

Offshore wind is an indigenous, clean, and inexhaustible source of energy. It is also an emerging industry, with strong potential for job creation. According to the prediction from National Renewable Energy Laboratory (NREL) in 2010, offshore wind could produce electricity for almost 39 million households by 2020 [55]. This figure could grow even faster beyond 2020, which would require advances in offshore wind turbine technology.

The current trend in wind energy is to go from land-based to offshore designs, where the latter include wind turbines with bottom-fixed foundation installed along the shoreline in relatively shallow depths, and wind turbines

mounted on a floating structure in deeper waters. Compared with land-based wind turbines, the floating offshore wind turbines have the following advantages: (a) The winds are stronger and more constant far from the shore, thus more energy can be generated; (b) The size of turbines is not limited by land transportation, provided the turbines can be assembled along the coastline and safely towed to their operating locations; (c) The visual and noise impact of wind turbines can be avoided due to operation far away from the shore; (d) Vast, open sea/ocean space is available. We believe that performing leading-edge wind energy research and development, which includes advanced fluid–structure interaction (FSI) modeling and simulation, will be essential in order to better exploit the above advantages of offshore wind in the future.

The current practice in simulating floating wind turbines makes use of either steady (time-independent), lumped-parameter aerodynamics and hydrodynamics models that are coupled with scaled down and/or simplified floating-wind-turbine structure models. These models are simple to implement and easy to execute, which makes them attractive, especially since they are routinely used as part of large parametric studies. However, because floating wind turbines are subjected to high wind speeds and violent sea states, and exhibit relatively complex mechanical response to wave loading, including mechanical components in relative motion superposed on elastic deformation of the blades and tower, these simplified models are often unable to adequately describe this behavior, especially in more extreme situations. Nevertheless, it is precisely these more

---

✉ Yuri Bazilevs  
yuri\_bazilevs@brown.edu

<sup>1</sup> School of Engineering, Brown University, 184 Hope St, Providence, RI 02912, USA

<sup>2</sup> Department of Civil and Environmental Engineering, University of Illinois at Urbana-Champaign, 1308 W Green St, Urbana, IL 61801, USA

<sup>3</sup> Department of Civil Engineering, The University of Hong Kong, Pok Fu Lam, Hong Kong

<sup>4</sup> Department of Mechanical and Manufacturing Engineering, University of Calgary, 40 Research Place, Calgary, AB T2L1Y6, Canada

extreme events that cause failures and reduce the remaining useful life of these machines, leading to premature maintenance and repair, and, as a result, to increased cost of offshore wind energy.

## 1.2 Role of Simulation and Experimental Measurements in Wind-Turbine Damage Prediction

Wind turbines operate for hundreds of millions of cycles during their lifetime. Due to cyclic loading, fatigue damage in blades, as well as in other wind-turbine structural and mechanical components, becomes an important issue. A thorough overview of the early techniques for wind-turbine fatigue-damage estimation may be found in [77], where it was noted that rigorous blade testing in a laboratory environment, as well as in real operating conditions, is necessary to develop realistic fatigue-damage forecasts. However, using experimental and field measurements from sensor data alone is not sufficient to accurately describe the structure damage initiation and progression. This is because sensor arrays typically produce signals from a limited number of spatial points, and, more importantly, the quantities measured do not directly quantify damage.

As the computational methods mature, high-fidelity models based on these methods are starting to be adopted for damage prognosis in large-scale structures [12, 42]. However, computational modeling alone is also not sufficient for making prediction about damage evolution because even the more sophisticated approaches contain many assumptions about geometry, material composition, constitutive modeling, boundary and initial conditions, etc., which do not always reflect physical reality.

Ideally, the computational model should be enriched, as much as possible, with sensor and measurements data that is used to periodically update the model inputs to maintain consistency with the measured data, and, thus, physical reality. Conversely, the appropriately updated computational model is, in turn, able to produce higher-fidelity outputs for the quantities directly linked to structural damage (e.g., the spatial damage-variable distribution), for which direct measurements are not available. This conceptual framework, in which sensor and measurement data for a given physical system co-exist in a symbiotic relationship with an advanced computational model of that system, is referred to as the Dynamic Data-Driven Application System (DDDAS) [30, 39]. As shown in recent work, DDDAS provides a pathway for accurate damage prediction in large-scale composite structures [12], and presents a new, important paradigm in other engineering applications [5, 6, 17, 21, 66].

## 1.3 Fatigue-Damage Modeling and Integration with FSI and DDDAS

Structures made of laminated composites, such as the wind-turbine blades, exhibit complex mechanical behavior [40] and, when it comes to fatigue-damage modeling, present significant challenges stemming from the multi-scale nature of the damage process [71, 78, 79]. The fatigue-damage model, proposed in [69, 70] and presented in this article, falls in the class of continuum damage models (CDMs) for fiber-reinforced composites, in which space- and time-dependent damage variables are evolved to quantitatively predict damage growth as a function of loading cycles [69, 70]. The model was deployed as part of the DDDAS framework to predict failure of a full-scale wind-turbine blade in a laboratory fatigue test in [12]. The model was also incorporated into FSI framework to predict fatigue damage in a full-scale Micon 65/13M wind turbine in [17].

Using standalone structural mechanics simulations, even in the presence of sensor data, is also insufficient for predicting fatigue damage growth in wind-turbine blades. As shown in [65], aerodynamic loading, and the structure response to that loading, contribute significantly to blade fatigue damage. However, it is virtually impossible to rigorously and accurately account for aerodynamic loading in laboratory fatigue tests. To increase the realism of the studies, one may attempt to study fatigue damage “in the field” as the turbines operate. However, wind-turbine blades are built to last hundreds of millions of cycles (here one cycle is assumed to be one full revolution of the rotor), and, unless premature blade failure occurs due to external factors, one needs to wait for upwards of a decade to see significant effects of fatigue damage, which is not practical. On the other hand, the blade fatigue-damage problem may be approached numerically, with the help of DDDAS, and using appropriate coupling of advanced FSI and CDM, which is what we present in this article.

## 1.4 FSI Modeling Techniques Employed

The FSI framework employed in the present paper was originally developed by the senior author in [13], and successfully applied to the simulation of horizontal- and vertical-axis wind turbines at full-scale in [13, 16, 17, 19, 46, 49, 63, 64]. For the fluid dynamics and turbulence modeling we make use of the variational multiscale (VMS) formulation [10] posed on a moving spatial domain using the Arbitrary Lagrangian–Eulerian (ALE) technique [51] with the addition of weakly-enforced no-slip boundary conditions [10, 15, 22] to improve coarse

boundary-layer mesh accuracy. This methodology was named ALE-VMS in [81].

It should be noted that VMS-based methods for fluid mechanics showed excellent results in many engineering applications involving turbulent flows, complex geometry, and moving domains - see references [14, 20, 23, 24, 26, 27, 56, 61, 64, 80, 82, 83, 91–97, 100, 118] for the examples of challenging computations performed using the VMS methodology in the context of ALE, space-time (ST), and fixed-grid techniques.

For FSI modeling of the floating offshore wind turbines, the level-set method [2–4, 57, 67, 68] is adopted to track the evolution of the free surface. The aerodynamics and hydrodynamics are governed by the Navier–Stokes equations of incompressible two-fluid flow, in which the fluid density and viscosity are evaluated with the aid of a level-set function.

The structural mechanics of wind turbines is modeled using Isogeometric Analysis (IGA) [34, 50], which is beneficial for the present application both from the standpoint of geometry modeling as well as accuracy. Since its conception, IGA has been widely used in many areas of computational mechanics, engineering and sciences, showing improved performance over the standard FEM [34]. The main structural components of on-land and offshore wind turbines, including blades, rotor, nacelle, tower and platform, are modeled as Kirchhoff–Love shells [29, 41, 58, 59] with the aid of the bending strip method [58], while the main shaft and mooring lines are modeled using the recently introduced rotation-free beam/cable formulation [72]. The IGA shell is used in the modeling of the wind-turbine composite blades, both as part of the FSI as well as fatigue-damage evolution simulations. For recent development in, and applications of, IGA the reader is referred to [7, 28, 31, 43–45, 47, 60, 72, 76, 115, 116].

The FSI methodology presented in this article assumes a non-matching discretization at the fluid–structure interface, which is handled by means of a recently-developed augmented Lagrangian FSI formulation with formal elimination of the Lagrange multiplier variable [13]. In the FSI formulation, the fluid–structure interface is tracked by the moving fluid mechanics mesh, while for the floating offshore wind turbines the air-water interface is captured (i.e., not tracked) on that mesh. In that sense, the method falls in the class of Mixed Interface-Tracking/Interface-Capturing Techniques (MITICT) [104, 107], which were primarily introduced for fluid–object interaction (FOI) with multiple fluids [86, 87]. To handle the added mass effect, which presents a challenge in the case of floating turbines, quasi-direct FSI coupling strategy [25, 84, 88, 90, 104, 109, 110, 112] is employed to solve the discrete FSI equations at each nonlinear iteration within a time step.

### 1.5 Outline

Governing equations of free-surface flows at the continuum and discrete levels are presented in Sects. 2 and 3, respectively. IGA-based structural mechanics formulation including a fatigue-damage model is presented in Sect. 4. Methods for time integration and FSI coupling for free-surface flows, and for the case of fatigue damage, are discussed in Sect. 5. FSI simulations employing the methods developed and reviewed in this article are shown in Sect. 6. In Sect. 7 we draw conclusions.

## 2 Continuum Formulation of Free-Surface Flows

In this section, the governing differential equations of free-surface flow on a moving domain are summarized. Let  $\Omega_t \in \mathbb{R}^d, d = 2, 3$  denote the combined air-water domain at time  $t$  and let  $\Gamma_t$  denote its boundary. The domain  $\Omega_t$  is decomposed into the water and air subdomains, denoted by  $\Omega_t^w$  and  $\Omega_t^a$ , respectively, and  $\Gamma_t^{aw}$  denotes the air-water interface. (See Fig. 1 for an illustration.)

In the present work, the level set method is adopted to capture the air-water interface. For this, we introduce a scalar function  $\phi(\mathbf{x}, t)$  and define the subdomains and their interface as follows:

$$\Omega_t^a = \{\mathbf{x} | \phi(\mathbf{x}, t) < 0, \forall \mathbf{x} \in \Omega_t\}, \tag{1}$$

$$\Omega_t^w = \{\mathbf{x} | \phi(\mathbf{x}, t) > 0, \forall \mathbf{x} \in \Omega_t\}, \tag{2}$$

$$\Gamma_t^{aw} = \{\mathbf{x} | \phi(\mathbf{x}, t) = 0, \forall \mathbf{x} \in \Omega_t\}. \tag{3}$$

In each subdomain, the fluid density  $\rho$  and viscosity  $\mu$  are defined as

$$\rho = \rho_w H(\phi) + \rho_a (1 - H(\phi)), \tag{4}$$

$$\mu = \mu_w H(\phi) + \mu_a (1 - H(\phi)), \tag{5}$$

where  $\rho_a$  and  $\rho_w$  are the constant densities of air and water, respectively,  $\mu_a$  and  $\mu_w$  are the constant viscosities of air

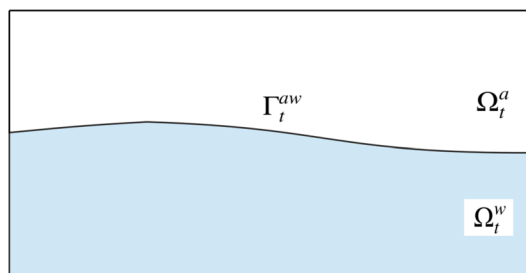


Fig. 1 Fluid mechanics spatial domain with air and water subdomains, and interface between them

and water, respectively, and  $H(\phi)$  is the Heaviside function expressed as

$$H(\phi) = \begin{cases} 0 & \text{if } \phi \leq 0, \\ 1/2 & \text{if } \phi = 0, \\ 1 & \text{if } \phi > 0. \end{cases} \tag{6}$$

With the fluid properties defined as above, the Navier–Stokes equations of incompressible two-fluid flow in the ALE description [51] may be written as follows:

$$\rho \left( \frac{\partial \mathbf{u}}{\partial t} \Big|_{\hat{x}} + (\mathbf{u} - \hat{\mathbf{u}}) \cdot \nabla \mathbf{u} - \mathbf{f} \right) - \nabla \cdot \sigma = \mathbf{0}, \tag{7}$$

$$\nabla \cdot \mathbf{u} = 0, \tag{8}$$

where the Cauchy stress tensor  $\sigma$  is defined as

$$\sigma(\mathbf{u}, p) = -p\mathbf{I} + 2\mu\nabla^s \mathbf{u}, \tag{9}$$

the fluid velocity and pressure are denoted by  $\mathbf{u}$  and  $p$ , respectively,  $\mathbf{f}$  is the body force per unit mass,  $\hat{\mathbf{u}}$  is the velocity of the fluid domain,  $\nabla^s$  is the symmetric gradient operator, and  $|_{\hat{x}}$  is used to denote the fact that the time derivative is taken with respect to a fixed referential domain (see [25] for more details).

The air-water interface is assumed to be convected by the flow, which is modeled by means of an additional convection equation of the level-set function  $\phi$  posed on a moving domain using the ALE description as follows:

$$\frac{\partial \phi}{\partial t} \Big|_{\hat{x}} + (\mathbf{u} - \hat{\mathbf{u}}) \cdot \nabla \phi = 0. \tag{10}$$

The above equations, together with the suitably chosen initial and boundary conditions, constitute the free-surface flow formulation on a moving domain at the continuous level.

### 3 Discrete Formulation of Free-Surface Flows

In this section we present the space-discrete version of the free-surface flow equations. We adopt the ALE-VMS formulation [14, 81–83], which has been applied to a variety of challenging fluid mechanics and FSI problems in [8, 16, 19, 20, 62, 63, 117], and also presented in the context of free-surface flow in [2–4, 57].

#### 3.1 ALE-VMS Formulation of Free-Surface Flow

Let  $\mathcal{V}^h$  denote the discrete trial space for the velocity-pressure-level set triple  $\{\mathbf{u}^h, p^h, \phi^h\}$ , and let  $\mathcal{W}^h$  denote the discrete test space for the linear-momentum, continuity and level-set equations  $\{\mathbf{w}^h, q^h, \eta^h\}$ . The ALE-VMS

formulation is stated as follows: Find  $\{\mathbf{u}^h, p^h, \phi^h\} \in \mathcal{V}^h$ , such that  $\forall \{\mathbf{w}^h, q^h, \eta^h\} \in \mathcal{W}^h$ :

$$\begin{aligned} & \int_{\Omega_t} \mathbf{w}^h \cdot \rho \left( \frac{\partial \mathbf{u}^h}{\partial t} \Big|_{\hat{x}} + (\mathbf{u}^h - \hat{\mathbf{u}}^h) \cdot \nabla \mathbf{u}^h - \mathbf{f}^h \right) d\Omega \\ & + \int_{\Omega_t} \nabla \mathbf{w}^h : \sigma(\mathbf{u}^h, p^h) d\Omega - \int_{\Gamma_t^h} \mathbf{w}^h \cdot \mathbf{h} d\Gamma \\ & + \sum_{e=1}^{n_{el}} \int_{\Omega_t^e} q^h \nabla \cdot \mathbf{u}^h d\Omega \\ & + \sum_{e=1}^{n_{el}} \int_{\Omega_t^e} \tau_M \left( (\mathbf{u}^h - \hat{\mathbf{u}}^h) \cdot \nabla \mathbf{w}^h + \frac{\nabla q^h}{\rho} \right) \cdot \mathbf{r}_M(\mathbf{u}^h, p^h) d\Omega \\ & + \sum_{e=1}^{n_{el}} \int_{\Omega_t^e} \rho \tau_C \nabla \cdot \mathbf{w}^h r_C(\mathbf{u}^h, p^h) d\Omega \\ & - \sum_{e=1}^{n_{el}} \int_{\Omega_t^e} \tau_M \mathbf{w}^h \cdot (\mathbf{r}_M(\mathbf{u}^h, p^h) \cdot \nabla \mathbf{u}^h) d\Omega \\ & - \sum_{e=1}^{n_{el}} \int_{\Omega_t^e} \frac{\nabla \mathbf{w}^h}{\rho} : (\tau_M \mathbf{r}_M(\mathbf{u}^h, p^h)) \otimes (\tau_M \mathbf{r}_M(\mathbf{u}^h, p^h)) d\Omega \\ & + \int_{\Omega_t} \eta^h \left( \frac{\partial \phi^h}{\partial t} \Big|_{\hat{x}} + (\mathbf{u}^h - \hat{\mathbf{u}}^h) \cdot \nabla \phi^h \right) d\Omega \\ & + \sum_{e=1}^{n_{el}} \int_{\Omega_t^e} \tau_\phi (\mathbf{u}^h - \hat{\mathbf{u}}^h) \cdot \nabla \eta^h \left( \frac{\partial \phi^h}{\partial t} \Big|_{\hat{x}} + (\mathbf{u}^h - \hat{\mathbf{u}}^h) \cdot \nabla \phi^h \right) d\Omega \\ & = 0. \end{aligned} \tag{11}$$

In Eq. (11),  $n_{el}$  is the number of elements in the domain,  $\mathbf{r}_M(\mathbf{u}^h, p^h)$  and  $r_C(\mathbf{u}^h, p^h)$  are element-interior residuals of the strong-form momentum and continuity equations, and  $\tau_M$ ,  $\tau_C$ , and  $\tau_\phi$  are the stabilization parameters [32, 48, 97, 99, 103, 105, 109].

To alleviate the high computational costs of detailed resolution of viscous turbulent boundary layers near solid surfaces without sacrificing the accuracy of hydrodynamic loading on structures, the ALE-VMS formulation of the level-set equations is augmented with weakly enforced no-slip boundary conditions. In this case, the following terms are added to the left hand side of Eq. (11):

$$\begin{aligned} & - \int_{\Gamma_t^g} \mathbf{w}^h \cdot \sigma(\mathbf{u}^h, p^h) \mathbf{n} d\Gamma \\ & - \int_{\Gamma_t^g} (2\mu \nabla^s \mathbf{w}^h \mathbf{n} + q^h \mathbf{n}) \cdot (\mathbf{u}^h - \mathbf{g}^h) d\Gamma \\ & - \int_{(\Gamma_t^g)^-} \mathbf{w}^h \cdot \rho ((\mathbf{u}^h - \hat{\mathbf{u}}^h) \cdot \mathbf{n}) (\mathbf{u}^h - \mathbf{g}^h) d\Gamma \\ & + \int_{\Gamma_t^g} \mathbf{w}^h \cdot \tau_B (\mathbf{u}^h - \mathbf{g}^h) d\Gamma. \end{aligned} \tag{12}$$

In Eq. (12),  $\mathbf{g}^h$  is the prescribed fluid velocity on the no-slip moving boundary  $\Gamma_t^g$ ,  $(\Gamma_t^g)^-$  denotes the inflow part of  $\Gamma_t^g$  and  $\tau_B$  is a boundary stabilization parameter. See [15, 22] for more details on weakly enforced essential boundary conditions, as well as more recent work in [98, 100] on

weakly enforced essential boundary conditions in the context of space–time methods.

### 3.2 Additional Level-Set Computational Technology

In discrete setting, the fluid density and viscosity are computed as

$$\rho = \rho_w H_\epsilon(\phi^h) + \rho_a(1 - H_\epsilon(\phi^h)), \tag{13}$$

$$\mu = \mu_w H_\epsilon(\phi^h) + \mu_a(1 - H_\epsilon(\phi^h)). \tag{14}$$

Here  $H_\epsilon(\phi)$  is a regularized version of the Heaviside function, namely,

$$H_\epsilon(\phi) = \begin{cases} 0 & \text{if } \phi < -\epsilon, \\ \frac{1}{2} \left( 1 + \frac{\phi}{\epsilon} + \frac{1}{\pi} \sin\left(\frac{\phi\pi}{\epsilon}\right) \right) & \text{if } |\phi| \leq \epsilon, \\ 1 & \text{if } \phi > \epsilon, \end{cases} \tag{15}$$

where  $\epsilon$ , assumed to scale with the local mesh size  $h$ , defines the interface width between the air and water subdomains.

While the regularized Heaviside function in Eq. (15) gives a smooth transition from zero to unity within a small band of elements around the interface, and is numerically more favorable to the sharp discontinuity, this regularization places a requirement on the level-set field  $\phi^h$  to satisfy the so-called signed-distance property in the transition layer between the two fluids. For this, we define an additional field,  $\phi_d^h$ , which satisfies the Eikonal partial differential equation, namely,

$$||\nabla\phi_d^h|| = 1 \text{ in } \Omega_t, \tag{16}$$

subject to the constraint that the interface defined by the zero level set of  $\phi^h$  is preserved, namely,

$$\phi_d^h = \phi^h = 0 \text{ on } \Gamma_t^{aw} \tag{17}$$

In order to satisfy Eqs. (16) and (17), we make the Eikonal equation “pseudo-time”-dependent (we denote pseudo-time by  $\tilde{t}$ ), discretize it using a VMS technique, and add a suitably-constructed penalty term to enforce the interior constraint on  $\phi_d^h$  given by Eq. (17). The resulting semi-discrete form of the governing equations may be stated as: Given  $\phi^h$ , find  $\phi_d^h$ , such that,  $\forall \eta_d^h$ ,

$$\begin{aligned} & \int_{\Omega_t} \eta_d^h \left( \frac{\partial \phi_d^h}{\partial \tilde{t}} + \mathbf{a} \cdot \nabla \phi_d^h - S_\epsilon(\phi^h) \right) d\Omega \\ & + \int_{\Omega_t} \tau_{\phi_d} \mathbf{a} \cdot \nabla \eta_d^h \left( \frac{\partial \phi_d^h}{\partial \tilde{t}} + \mathbf{a} \cdot \nabla \phi_d^h - S_\epsilon(\phi^h) \right) d\Omega \tag{18} \\ & + \int_{\Omega_t} \eta_d^h \lambda_{pen} \frac{dH_\epsilon(\phi^h)}{d\phi^h} (\phi_d^h - \phi^h) d\Omega = 0. \end{aligned}$$

Here  $S_\epsilon(\phi^h) = 2H_\epsilon(\phi^h) - 1$  is the regularized sign function,  $\mathbf{a} = S_\epsilon(\phi^h) \nabla \phi_d^h / ||\nabla \phi_d^h||$  is the effective “convective” velocity,  $\tau_{\phi_d}$  is the stabilization parameter, and  $\lambda_{pen}$  is the interface penalty parameter (see [3] for details). At each time step, Eq. (18) is integrated in pseudo-time, which gives a new level set field  $\phi_d^h$  with the signed-distance property and zero level set coincident with that of  $\phi^h$ . After this “re-distancing” process is done, we set  $\phi^h = \phi_d^h$  at the end of the time step.

*Remark* It is important to note that  $\frac{dH_\epsilon(\phi^h)}{d\phi^h}$  in Eq. (18) is only nonzero in a band of elements around the air-water interface, and thus the penalty term is only active near the air-water interface, which is the desired construction. Also note that the presence of  $\frac{dH_\epsilon(\phi^h)}{d\phi^h}$  produces the correct scaling of the penalty term and makes the penalty parameter  $\lambda_{pen}$  independent of the mesh size.

*Remark* Level set convection and re-distancing introduce mass balance errors, which accumulate as the equations are integrated in time. As a result, in the computations, a simple procedure is employed where the resultant re-distanced level-set field is perturbed by a constant to restore the mass balance. See [3] for details as well as additional references [1, 35–37, 57, 104, 106] where other mass correction techniques were proposed for free-surface flows.

## 4 Structural Mechanics Formulation

The structural mechanics formulation is based on the principle of virtual work. Let  $\mathcal{V}_s$  and  $\mathcal{W}_s$  denote the trial and test function sets for the structural mechanics problem. The principle of virtual work leads to the weak form of the structural mechanics problem, which may be stated as follows: Find  $\mathbf{d} \in \mathcal{V}_s$ , such that,  $\forall \mathbf{w}_s \in \mathcal{W}_s$ ,

$$\begin{aligned} & \int_{\Omega_0^s} \mathbf{w}_s \cdot \rho_s \left( \frac{d^2 \mathbf{d}}{dt^2} - \mathbf{f}_s \right) d\Omega + \int_{\Omega_0^s} \delta \mathbf{E} : \mathbf{S} d\Omega \\ & - \int_{\Gamma_0^s} \mathbf{w}_s \cdot \mathbf{h}_s d\Gamma = 0, \end{aligned} \tag{19}$$

where  $\mathbf{d}$  is the structural displacement,  $\rho_s$  is the density,  $\mathbf{E}$  is the Green–Lagrange strain tensor,  $\delta \mathbf{E}$  is its variation,  $\mathbf{S}$  is

the second Piola–Kirchhoff stress,  $\mathbf{f}_s$  is the body force per unit mass, and  $\mathbf{h}_s$  is the applied traction.

Since the structures simulated in this paper are essentially thin shells, we introduce the thin shell kinematics into the above weak formulation. Furthermore, in order to simulate laminated composite structures, we assume there are multiple plies through the shell thickness, each modeled as the St. Venant–Kirchhoff material. As a result, we obtain a Kirchhoff–Love shell formulation [59], which is written purely in terms of the shell midsurface displacements (i.e., the formulation is “rotation-free”), and which we discretize using IGA based on Non-Uniform Rational B-Splines (NURBS) [34, 50]. The weak formulation of the rotation-free isogeometric shell can be stated as: Find the shell midsurface displacement  $\mathbf{d}^h \in \mathcal{V}_s^h$ , such that,  $\forall \mathbf{w}_s^h \in \mathcal{W}_s^h$ ,

$$\begin{aligned} & \int_{\Gamma_t^s} \mathbf{w}_s^h \cdot \bar{\rho}_s h_{th} \left( \frac{d^2 \mathbf{d}^h}{dt^2} - \mathbf{f}_s \right) d\Gamma \\ & + \int_{\Gamma_0^s} \delta \bar{\epsilon}^h \cdot (\mathbf{K}_{exte} \bar{\epsilon}^h + \mathbf{K}_{coup} \bar{\kappa}^h) d\Gamma \\ & + \int_{\Gamma_0^s} \delta \bar{\kappa}^h \cdot (\mathbf{K}_{coup} \bar{\epsilon}^h + \mathbf{K}_{bend} \bar{\kappa}^h) d\Gamma \\ & + \int_{\Gamma_0^b} \delta \bar{\kappa}^h \cdot \mathbf{K}_{bend}^b \bar{\kappa}^h d\Gamma \\ & - \int_{\Gamma_0^s} \mathbf{w}_s^h \cdot \mathbf{h}_s d\Gamma = 0. \end{aligned} \tag{20}$$

In the above,  $\mathcal{V}_s^h$  and  $\mathcal{W}_s^h$  denote the trial and test function sets for the isogeometric shell formulation,  $\Gamma_0^s$  and  $\Gamma_t^s$  denote the shell midsurface in reference and current configuration, respectively,  $h_{th}$  is the local shell thickness,  $\bar{\epsilon}^h$  and  $\bar{\kappa}^h$  are the tensors of shell membrane strains and curvature changes expressed in Voigt notation and written with respect to the local basis oriented on the first covariant basis vector of the shell midsurface,  $\delta \bar{\epsilon}^h$  and  $\delta \bar{\kappa}^h$  are the corresponding variations.

Matrices  $\mathbf{K}_{exte}$ ,  $\mathbf{K}_{coup}$ , and  $\mathbf{K}_{bend}$  are the extensional, coupling, and bending stiffnesses, respectively, which, using the classical laminated plate theory [73], may be computed as follows:

$$\mathbf{K}_{exte} = \int_{h_{th}} \bar{\mathbf{C}} d\xi_3 = \sum_{k=1}^n \bar{\mathbf{C}}_k t_k, \tag{21}$$

$$\mathbf{K}_{coup} = \int_{h_{th}} \xi_3 \bar{\mathbf{C}} d\xi_3 = \sum_{k=1}^n \bar{\mathbf{C}}_k t_k \bar{z}_k, \tag{22}$$

$$\mathbf{K}_{bend} = \int_{h_{th}} \xi_3^2 \bar{\mathbf{C}} d\xi_3 = \sum_{k=1}^n \bar{\mathbf{C}}_k \left( t_k \bar{z}_k^2 + \frac{t_k^3}{12} \right). \tag{23}$$

Here  $\xi_3$  is the through-thickness coordinate,  $t_k$  denotes the thickness of the  $k^{\text{th}}$  ply,  $\bar{z}_k$  denotes its centroid, and  $\bar{\mathbf{C}}_k$  is a

constitutive material matrix for the  $k$ th ply in the local coordinate system computed as

$$\bar{\mathbf{C}}_k = \mathbf{T}^T(\phi_k) \tilde{\mathbf{C}}_k \mathbf{T}(\phi_k), \tag{24}$$

$$\mathbf{T}(\phi_k) = \begin{bmatrix} \cos^2 \phi_k & \sin^2 \phi_k & \sin \phi_k \cos \phi_k \\ \sin^2 \phi_k & \cos^2 \phi_k & -\sin \phi_k \cos \phi_k \\ -2 \sin \phi_k \cos \phi_k & 2 \sin \phi_k \cos \phi_k & \cos^2 \phi_k - \sin^2 \phi_k \end{bmatrix}, \tag{25}$$

where  $\mathbf{T}(\phi_k)$  is a transformation matrix defined by the fiber orientation angle in the ply  $\phi_k$ , and  $\tilde{\mathbf{C}}_k$  is the constitutive matrix for the orthotropic material written with respect to the principal material axes (or lamina axes) of the ply.

To enable modeling of structures comprised of multiple NURBS patches, and with regions of reduced continuity (e.g., sharp edges or non-manifold surfaces), the bending-strip technique is employed [58], which is expressed by means of the second-to-last term on the left-hand-side of Eq. (20). Here,  $\Gamma_0^b$  and  $\mathbf{K}_{bend}^b$  are the bending-strip domain in the shell reference configuration and the directional bending stiffness, respectively.

The shell model is augmented with a newly proposed isogeometric rotation-free bending-stabilized cable formulation [72], which may also be obtained by introducing the appropriate kinematics into the virtual-work principle given by Eq. (19), and reducing the formulation to the cable middle-curve displacement. The resulting weak formulation may be stated as: Find the middle curve displacement  $\mathbf{d}^h$ , such that,  $\forall \mathbf{w}_c^h$ ,

$$\begin{aligned} & \int_{S_0} \mathbf{w}_c^h \cdot \bar{\rho}_s A_0 \left( \frac{d^2 \mathbf{d}^h}{dt^2} - \mathbf{f}_s \right) dS \\ & + \int_{S_0} \delta \bar{\epsilon}_c^h [E_c A_0 ||\mathbf{G}'||^4] \bar{\epsilon}_c^h dS \\ & + \int_{S_0} \delta \bar{\kappa}_c^h [E_c I_0 ||\mathbf{G}'||^4] \bar{\kappa}_c^h dS = 0 \end{aligned} \tag{26}$$

In the above,  $S_0$  is the middle curve in reference configuration,  $A_0$  and  $I_0$  are the cable cross-section area and area moment of inertia, respectively,  $\bar{\epsilon}_c^h$  and  $\bar{\kappa}_c^h$  are the membrane strains and curvature changes written with respect to the basis vector oriented on the tangent vector to the middle curve, denoted by  $\mathbf{G}'$ ,  $\delta \bar{\epsilon}_c^h$  and  $\delta \bar{\kappa}_c^h$  are the corresponding variations, and  $E_c$  is the Young’s modulus.

### 4.1 Fatigue-Damage Model

The fatigue-damage model, proposed in [69, 70] and adapted to IGA-based Kirchhoff–Love shells in [12] is briefly recalled here. The ply-level constitutive matrix  $\tilde{\mathbf{C}}_k$  takes on the following form

$$\tilde{C}_k = \begin{bmatrix} \frac{E_1(1 - D_{11})}{1 - \nu_{21}\nu_{12}} & \frac{\nu_{21}E_1\sqrt{(1 - D_{11})(1 - D_{22})}}{1 - \nu_{21}\nu_{12}} & 0 \\ \frac{\nu_{12}E_2\sqrt{(1 - D_{11})(1 - D_{22})}}{1 - \nu_{21}\nu_{12}} & \frac{E_2(1 - D_{22})}{1 - \nu_{21}\nu_{12}} & 0 \\ 0 & 0 & \frac{G_{12}(1 - D_{12})}{1 - \nu_{21}\nu_{12}} \end{bmatrix}, \tag{27}$$

where  $\nu$ 's are the Poisson ratios,  $E_1$  and  $E_2$  are the Young's moduli in the fiber and matrix directions, respectively,  $G_{12}$  is the shear modulus, and  $D_{11}$ ,  $D_{22}$ , and  $D_{12}$  are, respectively, the fiber, matrix, and shear damage indices expressed as

$$D_{ij} = d_{ij}^t + d_{ij}^c \quad (i, j = 1, 2), \tag{28}$$

where  $d_{ij}^t$  and  $d_{ij}^c$  are the corresponding damage variables with the superscripts 't' and 'c' used to distinguish between tensile and compressive damage modes. For the case of high-cycle fatigue, assuming no damage growth occurs within the cycle, the evolution law for the damage variables is defined in terms of damage growth rate per cycle as

$$\frac{d(d_{ij}^{t,c})}{dN} = f(c_k, d_{ij}^{t,c}, D_{12}, \Sigma_{ij}) \quad (i, j = 1, 2), \tag{29}$$

where  $N$  denotes the cycle number, and reference [12] provides the detailed expressions for  $f$ . The damage growth rate is, in particular, an empirical function of material parameters  $c_k$  (total of nine parameters for fully-reversible cyclic loading) that govern damage initiation and propagation, and failure indices

$$\Sigma_{ij} = \frac{\Sigma_{ij}^{2D}}{1 + (\Sigma_{ij}^{2D} - \Sigma_{ij}^{1D})} \quad (i, j = 1, 2), \tag{30}$$

which can be seen as a combination of indices based on decoupled longitudinal, transverse, and shear failure modes ( $\Sigma_{ij}^{1D}$ 's), and indices based on the Tsai–Wu failure surface ( $\Sigma_{ij}^{2D}$ 's) wherein the failure modes are coupled [38].

## 5 FSI Coupling and Time Integration

### 5.1 Framework for Free-Surface Flow

The free-surface flow and IGA-based structural mechanics formulations are coupled as follows. In the Eq. (12), which details the weak no-slip boundary conditions for free-surface flow, the prescribed solid-wall velocity  $\mathbf{g}^h$  is replaced by the unknown structural displacement rate  $d\mathbf{h}^h/dt$  computed from the shell formulation given by Eq. (20). At the same time, the prescribed traction  $\mathbf{h}$ , in Eq. (20) is replaced

with the unknown traction field computed from the free-surface flow equations. Conservative fluid traction that is consistent with the weak enforcement of no-slip boundary conditions (see [9] for a definition) is employed in this work. Additional fluid-traction accuracy may be gained by employing a recently developed Separated Stress Projection (SSP) technique [85, 89, 101, 111, 113], where the pressure is projected as a scalar and viscous traction is projected as a vector quantity.

Application of the Generalized- $\alpha$  time integration technique [11, 33, 52] to the coupled free-surface FSI formulation leads to a coupled, nonlinear equation systems that need to be solved at every time step. To solve the nonlinear equation system, we employ the Newton–Raphson method, which requires solving a large linear-equation system that couples the different components of the free-surface FSI formulation. To increase the computational efficiency, we separate the linear system into “physics” and “mesh” subsystems, and solve them sequentially as follows. Increments of the fluid, level-set, and structure solution are obtained by solving a reduced linear system that couples these three fields. The new structure displacement is then used to update the fluid mechanics mesh configuration. The mesh deformation is governed by the equations of elastostatics with jacobian-based stiffening [53, 102, 104, 108, 109] to preserve the mesh quality. The overall approach may be classified as a quasi-direct FSI coupling technique [84, 88, 90, 104, 109, 110, 112], which is used here to handle the large fluid added mass present in the application.

In quasi-direct coupling, the off-diagonal tangent matrices are needed to solve the coupled linear system. In order to avoid assembling the off-diagonal terms, a flexible-GMRES (FGMRES) technique [74] with block-preconditioning is adopted. Application of the FGMRES technique to the solution of the coupled equation system requires computation of matrix-vector products, which are performed using a matrix-free technique. To precondition the FGMRES, we make use of the left-hand-side matrices of the individual fluid, level-set, and structure problems. The linear systems associated with preconditioning of the fluid and level-set equations are solved using a diagonally-scaled GMRES technique [75], while the structure problem is solved using a diagonally-scaled Conjugate Gradient

method. Other, more sophisticated preconditioning options may also be considered (see, e.g., [25]).

*Remark* While level-set convection is performed inside the Newton-iteration loop, level-set re-distancing and mass balance are performed once per time step. This is done from considerations of computational efficiency.

*Remark* We assume no coupling between the cables and surrounding fluid. Although the the cable cross-section is relatively small in the applications simulated, hydrodynamic loading on cables may be an important factor in the overall dynamics of the floating wind-turbine structures considered in this article. For this, a simple modification to the FSI formulation may consist in assuming one-way dependence, as in [114], wherein the cable is subjected to fluid drag forces, while the fluid does not “feel” the presence of the cable.

## 5.2 Algorithms for FSI Coupling with Fatigue Damage

Since we are interested in high-cycle fatigue for wind-turbine blades, and use a CDM formulation that assumes that damage growth occurs on a time scale that is much slower than a single rotor revolution, we feel it is sufficient to use a “frozen” damage state during FSI computations of the spinning rotor. This motivated the following overall algorithm:

1. We integrate the damage evolution law given by Eq. (29) using an explicit Euler method. Damage evolution is computed *at every Gaussian quadrature point of the blade surface and at each composite ply*. To enhance the computational efficiency, a “cycle-jump” technique is employed, where the stress state that drives the damage model is obtained by solving the coupled FSI system every NJUMP cycles of the damage evolution, where NJUMP is a user-controlled parameter.
2. Every time a new stress state is needed to integrate the damage-evolution equations, we perform a full dynamic FSI simulation for a time interval corresponding to a full (or partial) loading cycle, and extract the required stress data. The FSI equations are integrated in time using the Generalized- $\alpha$  method. As was reported in prior work on wind turbines, in the absence of free-surface flow, block-iterative FSI coupling strategy [25, 104, 109, 110, 112] is the most efficient choice for the present application [16].

While using the cycle-jump technique makes the problem computable, further reduction in computational time may be achieved by making the following observation: One rotor revolution may be decomposed into three  $120^\circ$  segments (see Fig. 2). As Blade 1 moves through zone I, Blade 2 moves through zone II, and Blade III moves through zone

III. Because gravity and rotor-stator interaction are taken into account, loads experienced by the blades in each zone differ in a significant manner. Nevertheless, the three blades moving through their respective zones collectively experience the same loading as a single blade undergoing a full revolution. As a result, we perform the FSI computation of a full machine with three blades for only  $1/3$  of a revolution every NJUMP cycles. However, when collecting blade-stress data to integrate the damage-evolution equations, time history of the stress from all three blades is employed.

*Remark* In the FSI calculations, the initial conditions chosen are often such that the coupled system undergoes unphysical transients, which eventually settle to produce a physical time-dependent response. In the present computations, in order to preclude this unphysical transient response from affecting the blade-damage evolution, in the beginning of the simulation, as well as after each NJUMP cycle, the FSI simulation is carried out for  $1/3$  of the revolution to ensure that the undesired transients settle.

## 6 Applications

### 6.1 Free-Surface FSI Simulations of an Offshore Floating Wind Turbine

In this section, we present a free-surface FSI simulation of an offshore floating wind turbine. The whole floating wind turbine consists of a supporting spar buoy called “Hywind”, developed by Statoil, and the NREL 5 MW baseline turbine. This design concept was chosen for its

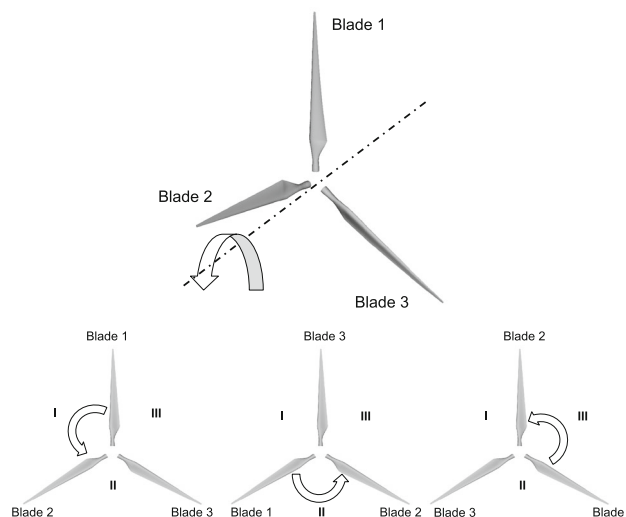


**Fig. 2** Decomposition of the rotor motion into three  $120^\circ$  segments. Simulation of the full machine with three blades for only  $1/3$  of the revolution is equivalent to simulating a single blade for a full revolution, from the standpoint of obtaining a full blade stress time history for driving the fatigue-damage model

suitability for modeling and existence of a full-scale prototype [54, 55]. The geometry of the complete floating structure is defined as follows. The rotor has a diameter of 126 m. The base of the tower is located at an elevation of 10 m above the still water level (SWL), while its top, which is coincident with the bottom of nacelle, is located at 87.6 m above the SWL. The centerline of the shaft passing through the center of the nacelle and hub corresponds to an elevation of 90 m. The tower is 3.87 m in diameter at the top and 6.5 m in diameter at the base. The latter dimension matches the diameter of the top of the floating platform. The platform consists of two cylindrical regions with depths of 14 m and 108 m, respectively, connected by a linearly tapered conical region with a depth of 8 m. The linearly tapered conical region extends from 4 to 12 m below the SWL. The base of the platform has a diameter of 9.4 m and is located at 120 m below the SWL. Three mooring cables are attached to the platform at 70 m below the SWL, and are anchored at the seabed at 320 m below the SWL. From the top view, the three cables, with the original length of 902 m, are distributed  $120^\circ$  apart. The whole floating system is depicted in Fig. 3. Additional geometry and material data for this turbine may be found in [119], which is the main source of the material presented in this section.

The main wind-turbine structural components, including the rotor, nacelle, tower and platform, are modeled using IGA Kirchhoff–Love shells. The bending strip technique [58] is adopted to deal with the multiple-patch discretization. The main shaft is modeled as a collection of beams, while mooring lines are modeled as cables. Quadratic NURBS are employed for both shell, beam and cable discretization. The total number of shell elements is 14,709, and a total number of beam/cable elements is 33. The fluid domain is meshed with tetrahedra and triangular prisms, and the number of nodes and elements in the simulations are 4,216,201 and 24,817,979 respectively. In addition, while the blades are flexible, the rotor is not allowed to spin in the FSI simulations presented.

First the simulation is performed by using the Airy-wave inflow conditions with zero mean flow, 6 m wave height and 156.13 m wave length. The time history of average platform displacement is plotted in Fig. 4. The simulation results obtained by NREL using the ADAMS code [54] are also plotted in Fig. 4 as a reference. Although the NREL data is obtained from a simulation of the no-rotor configuration, good agreement between the two simulations is nevertheless achieved. This is not surprising, since the rotor mass is low compared to the overall mass of the floating turbine. Furthermore, wind loading on the rotor is also very low due to zero-wind-speed conditions employed in the simulation.

Although linear wave theory like Airy wave is often used to model sea wave, it is insufficient to model more

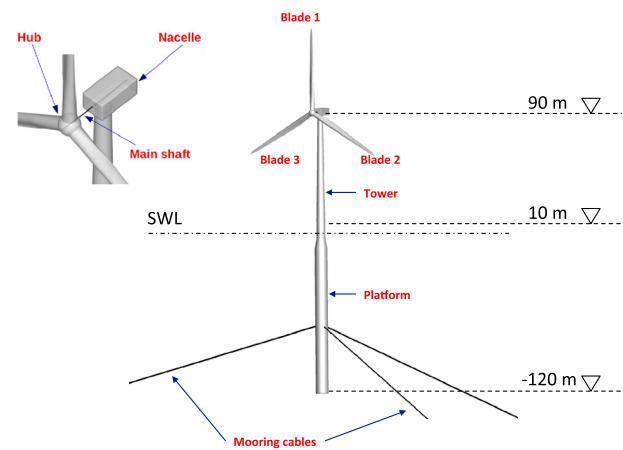


**Fig. 3** Structural model of the offshore floating wind turbine with zoom on the rotor

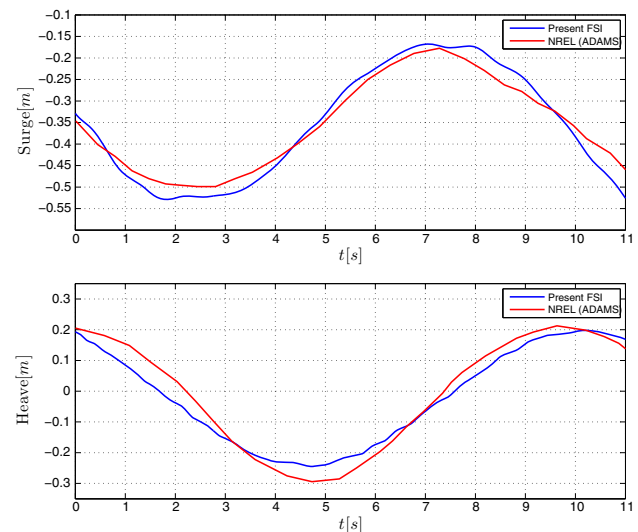
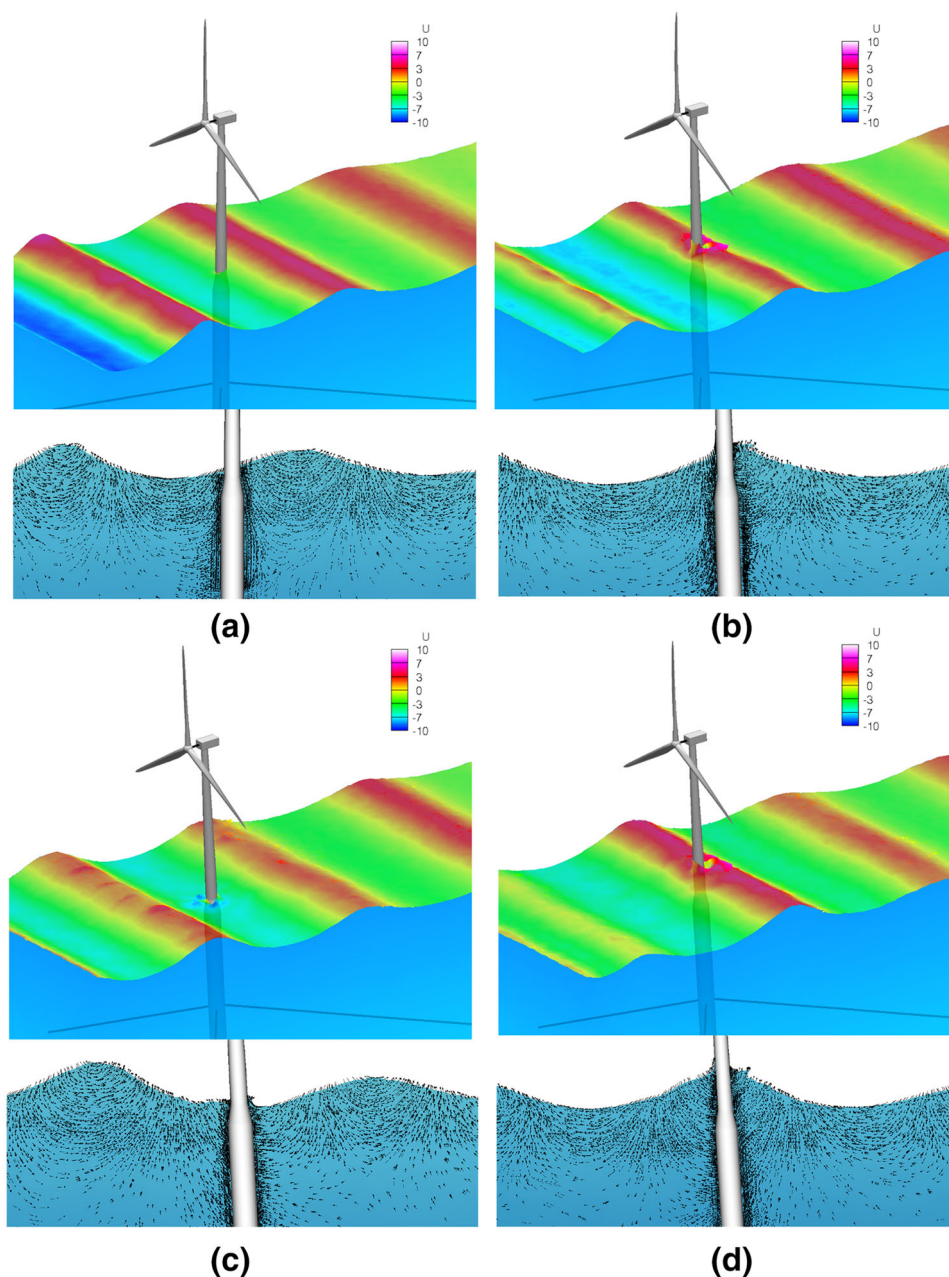


**Fig. 4** Platform center-of-mass displacement for Airy-wave conditions

“violent” sea conditions. To generate some more realistic waves, a piston-type wave generation concept, which is widely used in offshore engineering laboratories to generate irregular waves, is utilized numerically in this work. Considering that the free-surface flow formulation is proposed in a moving mesh, periodic horizontal motion of the inlet boundary is prescribed to mimic a piston motion. After the waves are generated, the wave profile is transferred from the numerical-wave-tank domain to the domain used for the FSI simulation of the floating wind turbine to carry out the FSI computation.

Figure 5 shows the wave surface colored by streamwise velocity and the corresponding velocity vector field in the water domain at different time instances. The wave peak height is about 18 m in this simulation. The configurations of the floating wind turbine are also shown in these two

**Fig. 5** Snapshots of free surface colored by streamwise velocity (in m/s) and the corresponding velocity field in the water domain at different time instants for piston-generated wave conditions



figures. Compared with Airy wave conditions, more complex free-surface phenomena, such as splashing, is observed when the waves impact the platform. In these stronger waves, the platform displacement is much bigger that can be observed in Fig. 4. We also plot the time history of the blade tip displacement for all three blades in Fig. 6 (see Fig. 3 for blade numbering). While the displacement time histories of blades 2 and 3 are very similar and relatively low in magnitude, blade 1, whose tip is at the highest point on the wind-turbine structure (over 90 m higher than the tips of blades 2 and 3), undergoes displacement with a more complex time history and much larger magnitude. The tip displacement time histories reveal the following

behavior. When the first wave peak reaches the turbine, the spar-buoy changes its direction of motion at a time instant of 3.7 s. The change in the direction of motion of the tips of blades 2 and 3 occurs at about 4.5 s, while blade 1 changes direction at about 4.8 s. This pattern repeats for other wave peaks.

## 6.2 FSI Modeling of Fatigue Damage in CX-100 Wind-Turbine Blades

We first deploy the DDDAS fatigue-damage framework on a full scale cantilever composite blade CX-100, which is calibrated by the measured acceleration data collected from

the indoor test [12]. The test blade was clamped at the root and driven by a hydraulic forcing with a natural frequency of 1.82 Hz of the first flap-wise bending mode. It was cyclically loaded until a fatigue-induced crack formed in the blade root region after about 8.0 M loading cycles. The accelerometers installed on the blade surface recorded the acceleration history. The blade mesh has 4647 quadratic NURBS elements. A time-periodic vertical displacement is applied at the blade root to mimic the hydraulic system forcing in the fatigue experiment. Two-DDDAS-loop scheme is devised to make use of the dynamic accelerometer data to update the computational model of the system. Figure 7 shows the predicted and measured

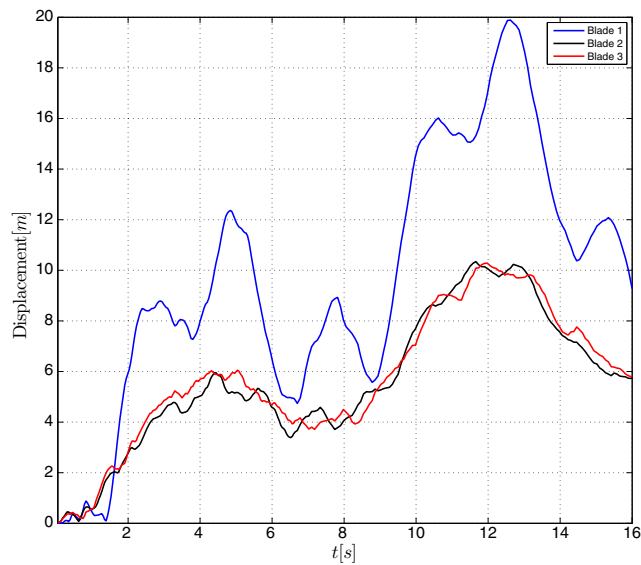


Fig. 6 Magnitude of tip displacement of three blades for piston-generated wave conditions

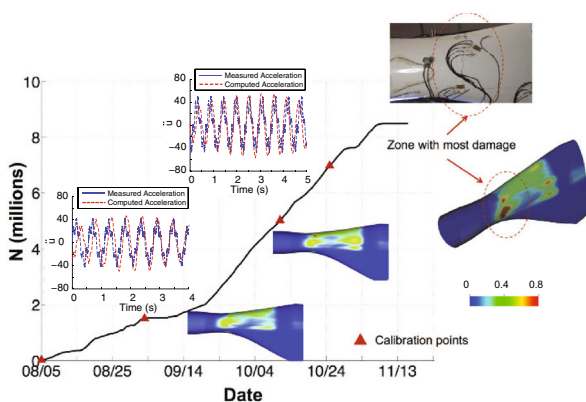


Fig. 7 Cycle count versus date for the fatigue test of the CX-100 blade. Triangular points indicate the calibration stations at which the simulation results for damage growth and acceleration history were compared to fatigue test data

accelerations in both time and frequency domains have good match. Excellent agreement between the location of the zone with most damage predicted by the simulation and the crack location observed in the fatigue test of the CX-100 composite blade is achieved, which may be seen in Fig. 7.

For the next step, we simulate fatigue damage “in the field” as the wind turbine operates. A coupled FSI and CDM simulation is carried out for the Micon 65/13M wind turbine mounted with Sandia CX-100 blades under realistic wind and rotor speed conditions [18]. This is a fixed-pitch, upwind horizontal-axis turbine with rated power of 100 kW. The wind-turbine rotor spins at 55 rpm and is subjected to a wind speed of 10.5 m/s. The fluid mesh consists of 2,877,958 linear elements, which are triangular prisms in the rotor boundary layers and tetrahedra elsewhere in the domain. The blade boundary-layer mesh has 15 layers of prismatic elements generated with a growth ratio of 1.2. The size of the first boundary-layer element in the wall-normal direction is 0.002 m. The time-step size is set to  $6.0 \times 10^{-5}$  s. Figure 8 shows the large blade tip deflection due to the overall softening of the blade by the time damage propagates through the blade, when the cycle count reaches 150 M. Compared to the the laboratory fatigue test, significant differences in damage patterns are observed for simulated realistic blade operating conditions (compare Figs. 7, 9.) This result underscores the importance of considering realistic structure loading when studying blade

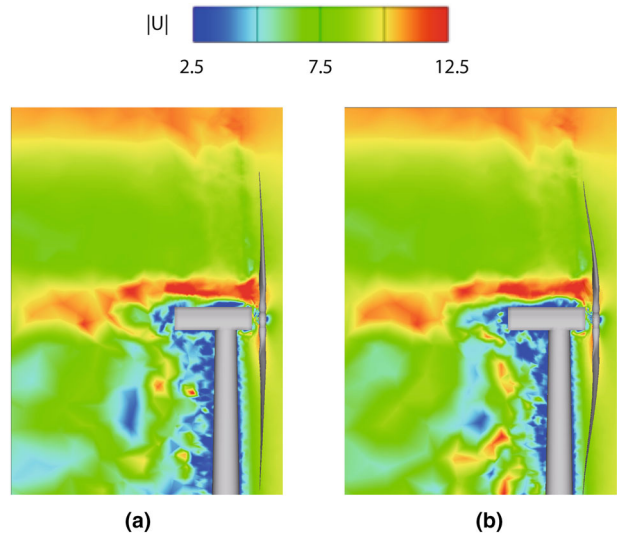
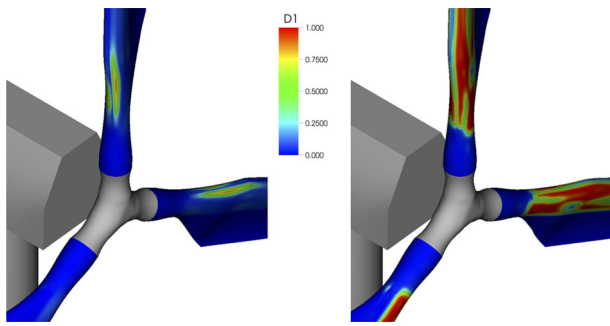


Fig. 8 Isocontours of air speed (in m/s) on a planar cut after 100,000 (left) and 150,000,000 (right) cycles. The right figure corresponds to the cycle right before the blade failure. Large blade tip deflection is due to significant loss of blade stiffness



**Fig. 9** Damage index  $D_1$  in the DBM-1708 layer near the blade aerodynamic zone after 100,000,000 (left) and 150,000,000 (right) cycles

fatigue damage, and employing advanced FSI in obtaining such loading data.

## 7 Concluding Remarks

This article focused on FSI simulation of floating wind turbines subjected to combined wind-flow and ocean-wave forcing, and on modeling of high-cycle fatigue failure of blades due to long-term cyclic aerodynamic loading. Computational techniques, including advanced structural modeling based on IGA, free-surface FSI, and fatigue-damage modeling, were reviewed. A DDDAS framework for steering FSI simulations of high-cycle fatigue damage in composite turbine blades was also presented. Representative computational examples involving land-based and floating offshore wind-turbine designs illustrate the versatility and power of the computational methods developed.

**Acknowledgements** We wish to thank the Texas Advanced Computing Center (TACC) and the San Diego Supercomputing Center (SDSC) for providing HPC resources that have contributed to the research results reported in this paper. YB and AK acknowledge the support of the AFOSR Award FA9550-16-1-0131.

**Funding** This work was partially funded by the AFOSR Award FA9550-16-1-0131.

## Compliance with Ethical Standards

**Conflict of interest** The authors declare that they have no conflict of interest.

## References

- Akin JE, Tezduyar TE, Ungor M (2007) Computation of flow problems with the mixed interface-tracking/interface-capturing technique (MITICT). *Comput Fluids* 36:2–11
- Akkerman I, Bazilevs Y, Benson DJ, Farthing MW, Kees CE (2012) Free-surface flow and fluid-object interaction modeling with emphasis on ship hydrodynamics. *J Appl Mech* 79:010905
- Akkerman I, Bazilevs Y, Kees CE, Farthing MW (2011) Iso-geometric analysis of free-surface flow. *J Comput Phys* 230:4137–4152
- Akkerman I, Dunaway J, Kvandal J, Spinks J, Bazilevs Y (2012) Toward free-surface modeling of planing vessels: simulation of the Fridsma hull using ALE-VMS. *Comput Mech* 50:719–727
- Allaire D, Biros G, Chambers J, Kordonow D, Ghattas O, Wilcox K (2012) Dynamic data driven methods for self-aware aerospace vehicles. *Proc Comput Sci* 9:1206–1210
- Allaire D, Chambers J, Cowlagi R, Kordonow D, Lecerf M, Mainini L, Ulker D, Wilcox K (2013) An offline/online dddd capability for self-aware aerospace vehicles. *Proc Comput Sci* 18:1959–1968
- Anitescu C, Yongjie Jessica Zhang YJ, Rabczuk T (2015) An isogeometric collocation method using superconvergent points. *Comput Methods Appl Mech Eng* 284:1073–1097
- Augier B, Yan J, Korobenko A, Czarnowski J, Ketterman G, Bazilevs Y (2015) Experimental and numerical FSI study of compliant hydrofoils. *Comput Mech* 55:1079–1090
- Bazilevs Y, Akkerman I (2010) Large eddy simulation of turbulent Taylor–Couette flow using isogeometric analysis and the residual-based variational multiscale method. *J Comput Phys* 229:3402–3414
- Bazilevs Y, Calo VM, Cottrell JA, Hughes TJR, Reali A, Scovazzi G (2007) Variational multiscale residual-based turbulence modeling for large eddy simulation of incompressible flows. *Comput Methods Appl Mech Eng* 197:173–201
- Bazilevs Y, Calo VM, Hughes TJR, Zhang Y (2008) Isogeometric fluid–structure interaction: theory, algorithms, and computations. *Comput Mech* 43:3–37
- Bazilevs Y, Deng X, Korobenko A, Lanza di Scalea F, Todd MD, Taylor SG (2015) Isogeometric fatigue damage prediction in large-scale composite structures driven by dynamic sensor data. *J Appl Mech* 82:091008–091008–12
- Bazilevs Y, Hsu M-C, Scott MA (2012) Isogeometric fluid–structure interaction analysis with emphasis on non-matching discretizations, and with application to wind turbines. *Comput Methods Appl Mech Eng* 249–252:28–41
- Bazilevs Y, Hsu M-C, Takizawa K, Tezduyar TE (2012) ALE-VMS and ST-VMS methods for computer modeling of wind-turbine rotor aerodynamics and fluid–structure interaction. *Mathem Models Methods Appl Sci* 22(supp02):1230002
- Bazilevs Y, Hughes TJR (2007) Weak imposition of Dirichlet boundary conditions in fluid mechanics. *Comput Fluids* 36:12–26
- Bazilevs Y, Korobenko A, Deng X, Yan J (2015) Novel structural modeling and mesh moving techniques for advanced FSI simulation of wind turbines. *Int J Numer Methods Eng* 102:766–783
- Bazilevs Y, Korobenko A, Deng X, Yan J (2016) Fluid-structure interaction modeling for fatigue-damage prediction in full-scale wind-turbine blades. *J Appl Mech* 83(6):061010
- Bazilevs Y, Korobenko A, Deng X, Yan J (2016) FSI modeling for fatigue-damage prediction in full-scale wind-turbine blades. *J Appl Mech* 83(6):061010
- Bazilevs Y, Korobenko A, Deng X, Yan J, Kinzel M, Dabiri JO (2014) FSI modeling of vertical-axis wind turbines. *J Appl Mech* 81:081006
- Bazilevs Y, Korobenko A, Yan J, Pal A, Gohari SMI, Sarkar S (2015) ALE-VMS formulation for stratified turbulent incompressible flows with applications. *Math Models Methods Appl Sci* 25(12):2349–2375

21. Bazilevs Y, Marsden AL, Lanza di Scalea F, Majumdar A, Tatineni M (2012) Toward a computational steering framework for large-scale composite structures based on continually and dynamically injected sensor data. *Proc Comput Sci* 9:1149–1158
22. Bazilevs Y, Michler C, Calo VM, Hughes TJR (2010) Isogeometric variational multiscale modeling of wall-bounded turbulent flows with weakly enforced boundary conditions on unstretched meshes. *Comput Methods Appl Mech Eng* 199:780–790
23. Bazilevs Y, Takizawa K, Tezduyar TE (2013) Challenges and directions in computational fluid–structure interaction. *Math Models Methods Appl Sci* 23:215–221
24. Bazilevs Y, Takizawa K, Tezduyar TE (2015) New directions and challenging computations in fluid dynamics modeling with stabilized and multiscale methods. *Math Models Methods Appl Sci* 25:2217–2226
25. Bazilevs Y, Takizawa K, Tezduyar TE (2013) *Computational fluid–structure interaction: methods and applications*. Wiley, London
26. Bazilevs Y, Takizawa K, Tezduyar TE, Hsu M-C, Kostov N, McIntyre S (2014) Aerodynamic and FSI analysis of wind turbines with the ALE-VMS and ST-VMS methods. *Arch Comput Methods Eng* 21:359–398
27. Bazilevs Y, Yan J, de Stadler M, Sarkar S (2014) Computation of the flow over a sphere at  $Re = 3700$ : a comparison of uniform and turbulent inflow conditions. *J Appl Mech* 81(12):121003
28. Beir Da Veiga L, Hughes TJR, Kiendl J, Lovadina C, Niiranen J, Reali A, Speleers H (2015) A locking-free model for Reissner–Mindlin plates: analysis and isogeometric implementation via nurbs and triangular nurps. *Math Models Methods Appl Sci* 28:1519–1551
29. Benson DJ, Bazilevs Y, Hsu M-C, Hughes TJR (2011) A large deformation, rotation-free, isogeometric shell. *Comput Methods Appl Mech Eng* 200:1367–1378
30. Blasch E, Ravela S, Aved A (eds) (2019) *Handbook of dynamic data driven applications systems*. Springer, Berlin
31. Borden MJ, Hughes TJR, Landis CM, Verhoosel CV (2014) A higher-order phase-field model for brittle fracture: formulation and analysis within the isogeometric analysis framework. *Comput Methods Appl Mech Eng* 273:100–118
32. Brooks AN, Hughes TJR (1982) Streamline upwind/Petrov–Galerkin formulations for convection dominated flows with particular emphasis on the incompressible Navier–Stokes equations. *Comput Methods Appl Mech Eng* 32:199–259
33. Chung J, Hulbert GM (1993) A time integration algorithm for structural dynamics with improved numerical dissipation: the generalized- $\alpha$  method. *J Appl Mech* 60:371–75
34. Cottrell JA, Hughes TJR, Bazilevs Y (2009) *Isogeometric analysis. Toward integration of CAD and FEA*. Wiley, London
35. Cruchaga M, Celentano D, Tezduyar T (2001) A moving Lagrangian interface technique for flow computations over fixed meshes. *Comput Methods Appl Mech Eng* 191:525–543
36. Cruchaga M, Celentano D, Tezduyar T (2002) Computation of mould filling processes with a moving Lagrangian interface technique. *Commun Numer Methods Eng* 18:483–493
37. Cruchaga MA, Celentano DJ, Tezduyar TE (2005) Moving-interface computations with the edge-tracked interface locator technique (ETILT). *Int J Numer Methods Fluids* 47:451–469
38. Daniel IM, Ishai O (2006) *Engineering mechanics of composite materials*. Oxford University Press, Oxford
39. Darema F (2004) Dynamic data driven applications systems: a new paradigm for application simulations and measurements. In: *Proceedings of ICCS 2004 4th international conference on computational science*, pp 662–669
40. Degrieck J, Paepegem WV (2001) Fatigue damage modelling of fiber-reinforced composite materials: review. *Appl Mech Rev* 54(4):279–300
41. Echter R, Oesterle B, Bischoff M (2013) A hierarchic family of isogeometric shell finite elements. *Comput Methods Appl Mech Eng* 254:170–180
42. Griffith TD (2015) *Structural health and prognostics management for offshore wind plants: final report of sandia research and developments activities*. Report of the Sandia National Laboratory
43. Guo Y, Ruess M (2015) A layerwise isogeometric approach for nurbs-derived laminate composite shells. *Compos Struct* 124:300–309
44. Hillman M, Chen JS, Bazilevs Y (2015) Variationally consistent domain integration for isogeometric analysis. *Comput Methods Appl Mech Eng* 284:521–540
45. Hosseini S, Remmers JJC, Verhoosel CV, de Borst R (2015) Propagation of delamination in composite materials with isogeometric continuum shell elements. *Int J Numer Methods Eng* 102:159–179
46. Hsu M-C, Bazilevs Y (2012) Fluid–structure interaction modeling of wind turbines: simulating the full machine. *Comput Mech* 50:821–833
47. Hsu M-C, Wang C, Herrema AJ, Schillinger D, Ghoshal A, Bazilevs Y (2015) An interactive geometry modeling and parametric design platform for isogeometric analysis. *Comput Math Appl* 70:1481–1500
48. Hsu M-C, Bazilevs Y, Calo VM, Tezduyar TE, Hughes TJR (2010) Improving stability of stabilized and multiscale formulations in flow simulations at small time steps. *Comput Methods Appl Mech Eng* 199:828–840
49. Hsu M-C, Kamensky D, Bazilevs Y, Sacks MS, Hughes TJR (2014) Fluid–structure interaction analysis of bioprosthetic heart valves. *Comput Mech* 54:1055–1071
50. Hughes TJR, Cottrell JA, Bazilevs Y (2005) Isogeometric analysis: CAD, finite elements, NURBS, exact geometry, and mesh refinement. *Computer Methods in Applied Mechanics and Engineering* 194:4135–4195
51. Hughes TJR, Liu WK, Zimmermann TK (1981) Lagrangian–Eulerian finite element formulation for incompressible viscous flows. *Comput Methods Appl Mech Eng* 29:329–349
52. Jansen KE, Whiting CH, Hulbert GM (2000) A generalized- $\alpha$  method for integrating the filtered Navier–Stokes equations with a stabilized finite element method. *Comput Methods Appl Mech Eng* 190:305–319
53. Johnson AA, Tezduyar TE (1994) Mesh update strategies in parallel finite element computations of flow problems with moving boundaries and interfaces. *Comput Methods Appl Mech Eng* 119:73–94
54. Jonkman J, Musial W (2010) *Offshore code comparison collaboration (OC3) for IEA task 23 offshore wind technology and deployment*. NREL Technical Report
55. Jonkman JM (2010) *Definition of the floating system for phase IV of OC3*. National Renewable Energy Laboratory Golden, Golden
56. Kamensky D, Hsu M-C, Schillinger D, Evans JA, Aggarwal A, Bazilevs Y, Sacks MS, Hughes TJR (2015) An immersed isogeometric variational framework for fluid–structure interaction: application to bioprosthetic heart valves. *Comput Methods Appl Mech Eng* 284:1005–1053
57. Kees CE, Akkerman I, Farthing MW, Bazilevs Y (2011) A conservative level set method suitable for variable-order approximations and unstructured meshes. *J Comput Phys* 230:4536–4558
58. Kiendl J, Bazilevs Y, Hsu M-C, Wüchner R, Bletzinger K-U (2010) The bending strip method for isogeometric analysis of

- Kirchhoff–Love shell structures comprised of multiple patches. *Comput Methods Appl Mech Eng* 199:2403–2416
59. Kiendl J, Bletzinger K-U, Linhard J, Wüchner R (2009) Isogeometric shell analysis with Kirchhoff–Love elements. *Comput Methods Appl Mech Eng* 198:3902–3914
  60. Kiendl J, Hsu M-C, Wu MCH, Reali A (2015) Isogeometric Kirchhoff–Love shell formulations for general hyperelastic materials. *Comput Methods Appl Mech Eng* 291:280–303
  61. Korobenko A, Hsu M-C, Akkerman I, Bazilevs Y (2013) Aerodynamic simulation of vertical-axis wind turbines. *J Appl Mech* 81(2):021011
  62. Korobenko A, Hsu M-C, Akkerman I, Bazilevs Y (2013) Aerodynamic simulation of vertical-axis wind turbines. *J Appl Mech* 81:021011
  63. Korobenko A, Hsu M-C, Akkerman I, Tippmann J, Bazilevs Y (2013) Structural mechanics modeling and FSI simulation of wind turbines. *Math Models Methods Appl Sci* 23:249–272
  64. Korobenko A, Yan J, Gohari SMI, Sarkar S, Bazilevs Y (2017) FSI simulation of two back-to-back wind turbines in atmospheric boundary layer flow. *Comput Fluids* 158:167–175
  65. Lee S, Churchfield M, Moriarty P, Jonkman J, Michalakes J (2012) Atmospheric and wake turbulence impacts on wind turbine fatigue loading. Conference Paper presented at 50th AIAA Aerospace Sciences Meeting, Nashville, Tennessee
  66. Oden JT, Diller KR, Bajaj C, Browne JC, Hazle J, Babuska I, Bass J, Demkowicz L, Feng Y, Fuentes D, Prudhomme S, Rylander MN, Stafford RJ, Zhang Y (2007) Dynamic data-driven finite element models for laser treatment of prostate cancer. *Numer Methods PDE* 23:904–922
  67. Osher S, Fedkiw R (2006) Level set methods and dynamic implicit surfaces, vol 153. Springer, Berlin
  68. Osher S, Sethian JA (1988) Fronts propagating with curvature-dependent speed: algorithms based on Hamilton–Jacobi formulations. *J Comput Phys* 79(1):12–49
  69. Paepegem WV, Degrieck J (2002) A new coupled approach of residual stiffness and strength for fatigue of fiber-reinforced composites. *Int J Fatigue* 24:747–762
  70. Paepegem WV, Degrieck J (2004) Simulating in-plane fatigue damage in woven glass fibre-reinforced composites subject to fully reversed cyclic loading. *Fatigue Fract Eng Mater Struct* 27:1197–1208
  71. Raghavan P, Li S, Ghosh S (2004) Two scale response and damage modeling of composite materials. *Finite Elem Anal Design* 40:1619–1640
  72. Raknes SB, Deng X, Bazilevs Y, Benson DJ, Mathisen KM, Kvamsdal T (2013) Isogeometric rotation-free bending-stabilized cables: statics, dynamics, bending strips and coupling with shells. *Comput Methods Appl Mech Eng* 263:127–143
  73. Reddy JN (2004) *Mechanics of laminated composite plates and shells: theory and analysis*, 2nd edn. CRC Press, Boca Raton
  74. Saad Y (1993) A flexible inner-outer preconditioned GMRES algorithm. *SIAM J Sci Comput* 14(2):461–469
  75. Saad Y, Schultz M (1986) GMRES: a generalized minimal residual algorithm for solving nonsymmetric linear systems. *SIAM J Sci Stat Comput* 7:856–869
  76. Schilling D, Borden MJ, Stolarski HK (2015) Isogeometric collocation for phase-field fracture models. *Comput Methods Appl Mech Eng* 284:583–610
  77. Sutherland HJ (1999) On the fatigue analysis of wind turbines. Report of the Sandia National Laboratory
  78. Swaminathan S, Ghosh S (2006) Statistically equivalent representative volume elements for composite microstructures, part ii: with evolving damage. *J Compos Mater* 40:605–621
  79. Swaminathan S, Ghosh S, Pagano NJ (2006) Statistically equivalent representative volume elements for composite microstructures, part i: without damage. *J Compos Mater* 40:583–604
  80. Takizawa K (2014) Computational engineering analysis with the new-generation space–time methods. *Comput Mech* 54:193–211
  81. Takizawa K, Bazilevs Y, Tezduyar TE (2012) Space–time and ALE-VMS techniques for patient-specific cardiovascular fluid–structure interaction modeling. *Arch Comput Methods Eng* 19:171–225
  82. Takizawa K, Bazilevs Y, Tezduyar TE, Hsu M-C, Øiseth O, Mathisen KM, Kostov N, McIntyre S (2014) Engineering analysis and design with ALE-VMS and space–time methods. *Arch Comput Methods Eng* 21:481–508
  83. Takizawa K, Bazilevs Y, Tezduyar TE, Long CC, Marsden AL, Schjodt K (2014) ST and ALE-VMS methods for patient-specific cardiovascular fluid mechanics modeling. *Math Models Methods Appl Sci* 24:2437–2486
  84. Takizawa K, Montes D, Fritze M, McIntyre S, Boben J, Tezduyar TE (2013) Methods for FSI modeling of spacecraft parachute dynamics and cover separation. *Math Models Methods Appl Sci* 23:307–338
  85. Takizawa K, Moorman C, Wright S, Spielman T, Tezduyar TE (2011) Fluid–structure interaction modeling and performance analysis of the Orion spacecraft parachutes. *Int J Numer Methods Fluids* 65:271–285
  86. Takizawa K, Tanizawa K, Yabe T, Tezduyar TE (2007) Computational ship hydrodynamics with the CIP method. In Onate E, Garcia J, Bergan P, Kvamsdal T (eds) *Marine 2007*, Barcelona, Spain, CIMNE
  87. Takizawa K, Tanizawa K, Yabe T, Tezduyar TE (2007) Ship hydrodynamics computations with the CIP method based on adaptive Soroban grids. *Int J Numer Methods Fluids* 54:1011–1019
  88. Takizawa K, Tezduyar TE (2011) Multiscale space–time fluid–structure interaction techniques. *Comput Mech* 48:247–267
  89. Takizawa K, Tezduyar TE (2012) Computational methods for parachute fluid–structure interactions. *Arch Comput Methods Eng* 19:125–169
  90. Takizawa K, Tezduyar TE (2012) Space–time fluid–structure interaction methods. *Math Models Methods Appl Sci* 22(supp02):1230001
  91. Takizawa K, Tezduyar TE, Boben J, Kostov N, Boswell C, Buscher A (2013) Fluid–structure interaction modeling of clusters of spacecraft parachutes with modified geometric porosity. *Comput Mech* 52:1351–1364
  92. Takizawa K, Tezduyar TE, Boswell C, Kolesar R, Montel K (2014) FSI modeling of the reefed stages and disreefing of the Orion spacecraft parachutes. *Comput Mech* 54:1203–1220
  93. Takizawa K, Tezduyar TE, Buscher A (2015) Space–time computational analysis of MAV flapping-wing aerodynamics with wing clapping. *Comput Mech* 55:1131–1141
  94. Takizawa K, Tezduyar TE, Kolesar R (2015) FSI modeling of the Orion spacecraft drogue parachutes. *Comput Mech* 55:1167–1179
  95. Takizawa K, Tezduyar TE, Kolesar R, Boswell C, Kanai T, Montel K (2014) Multiscale methods for gore curvature calculations from FSI modeling of spacecraft parachutes. *Comput Mech* 54:1461–1476
  96. Takizawa K, Tezduyar TE, Kostov N (2014) Sequentially-coupled space–time FSI analysis of bio-inspired flapping-wing aerodynamics of an MAV. *Comput Mech* 54:213–233
  97. Takizawa K, Tezduyar TE, Kuraishi T (2015) Multiscale ST methods for thermo-fluid analysis of a ground vehicle and its tires. *Math Models Methods Appl Sci* 25:2227–2255
  98. Takizawa K, Tezduyar TE, Kuraishi T, Tabata S, Takagi H (2016) Computational thermo-fluid analysis of a disk brake. *Comput Mech* 57:965–977

99. Takizawa K, Tezduyar TE, McIntyre S, Kostov N, Kolesar R, Habluetzel C (2014) Space–time VMS computation of wind-turbine rotor and tower aerodynamics. *Comput Mech* 53:1–15
100. Takizawa K, Tezduyar TE, Mochizuki H, Hattori H, Mei S, Pan L, Montel K (2015) Space–time VMS method for flow computations with slip interfaces (ST-SI). *Math Models Methods Appl Sci* 25:2377–2406
101. Takizawa K, Wright S, Moorman C, Tezduyar TE (2011) Fluid–structure interaction modeling of parachute clusters. *Int J Numer Methods Fluids* 65:286–307
102. Tezduyar T, Aliabadi S, Behr M, Johnson A, Mittal S (1993) Parallel finite-element computation of 3D flows. *Computer* 26(10):27–36
103. Tezduyar T, Sathe S (2003) Stabilization parameters in SUPG and PSPG formulations. *J Comput Appl Mech* 4:71–88
104. Tezduyar TE (2001) Finite element methods for flow problems with moving boundaries and interfaces. *Arch Comput Methods Eng* 8:83–130
105. Tezduyar TE (2003) Computation of moving boundaries and interfaces and stabilization parameters. *Int J Numer Methods Fluids* 43:555–575
106. Tezduyar TE (2007) Finite elements in fluids: special methods and enhanced solution techniques. *Comput Fluids* 36:207–223
107. Tezduyar TE (2007) Finite elements in fluids: stabilized formulations and moving boundaries and interfaces. *Comput Fluids* 36:191–206
108. Tezduyar TE, Behr M, Mittal S, Johnson AA (1992) Computation of unsteady incompressible flows with the finite element methods: space–time formulations, iterative strategies and massively parallel implementations. In: *New methods in transient analysis*, PVP-Vol.246/AMD-Vol.143, pp 7–24. ASME, New York
109. Tezduyar TE, Sathe S (2007) Modeling of fluid–structure interactions with the space–time finite elements: solution techniques. *Int J Numer Methods Fluids* 54:855–900
110. Tezduyar TE, Sathe S, Keedy R, Stein K (2006) Space–time finite element techniques for computation of fluid–structure interactions. *Comput Methods Appl Mech Eng* 195:2002–2027
111. Tezduyar TE, Sathe S, Pausewang J, Schwaab M, Christopher J, Crabtree J (2008) Interface projection techniques for fluid–structure interaction modeling with moving-mesh methods. *Comput Mech* 43:39–49
112. Tezduyar TE, Sathe S, Stein K (2006) Solution techniques for the fully-discretized equations in computation of fluid–structure interactions with the space–time formulations. *Comput Methods Appl Mech Eng* 195:5743–5753
113. Tezduyar TE, Takizawa K, Brummer T, Chen PR (2011) Space–time fluid–structure interaction modeling of patient-specific cerebral aneurysms. *Int J Numer Methods Biomed Eng* 27:1665–1710
114. Tezduyar TE, Takizawa K, Moorman C, Wright S, Christopher J (2010) Space–time finite element computation of complex fluid–structure interactions. *Int J Numer Methods Fluids* 64:1201–1218
115. Valizadeh N, Bazilevs Y, Chen JS, Rabczuk T (2015) A coupled IGA-Meshfree discretization of arbitrary order of accuracy and without global geometry parametrization. *Comput Methods Appl Mech Eng* 293:20–37
116. van Opstal T, Fonn E, Holdahl R, Kvamsdal T, Kvarving AM, Mathisen KM, Nordanger K, Okstad KM, Rasheed A, Tabib M (2015) Isogeometric methods for CFD and FSI-simulation of flow around turbine blades. *Energy Proc* 80:442–449
117. Yan J, Augier B, Korobenko A, Czarnowski J, Ketterman G, Bazilevs Y (2016) FSI modeling of a propulsion system based on compliant hydrofoils in a tandem configuration. *Comput Fluids* 141:201–211
118. Yan J, Deng X, Korobenko A, Bazilevs Y (2017) Free-surface flow modeling and simulation of horizontal-axis tidal-stream turbines. *Comput Fluids*, Published online. <https://doi.org/10.1016/j.compfluid.2016.06.016>
119. Yan J, Korobenko A, Deng X, Bazilevs Y (2016) Computational free-surface fluid–structure interaction with application to floating offshore wind turbines. *Comput Fluids* 141:155–174